

Fully exposed copper single-atom sites on mesoporous N/S-codoped graphene for efficient zinc-air battery

Lifen Yang^{*}, Changliang Du, Jiachen Tian, Xiuyun Yao, Qianwei Zhang, Xilan Ma, Youqi Zhu^{*}, Meishuai Zou^{*}, Chuanbao Cao^{*}

Research Center of Materials Science, Beijing Key Laboratory of Construction Tailorable Advanced Functional Materials and Green Applications, Beijing Institute of Technology, Beijing 100081, China



ARTICLE INFO

Keywords:
Single-atom catalysts
Graphene
Mesoporous structure
Oxygen reduction reaction
Zn-air battery

ABSTRACT

Transition metal single-atom catalysts are recently emerging as the most potential candidates for the oxygen reduction reaction due to their remarkable activity and durability, yet subjected to limited availability proportion of active sites to reactant in practice due to the lack of favorable morphology. Herein, the ultrathin mesoporous N/S-codoped graphene is fabricated by a potassium thiocyanate (KSCN) assisted pyrolysis of metal-organic framework (ZIF-8) as the robust substrate for anchoring copper single-atom sites. The KSCN-assisted pyrolysis can not only create N and S coordination atoms but also regulate the fully exposed morphology. The graphene-supported copper single-atom catalysts (g-Cu-SACs) show typical mesoporous structure with larger surface area of $1612 \text{ m}^2 \text{ g}^{-1}$. Spectral and microscopy results reveal highly isolated Cu single-atom sites on mesoporous graphene with unsymmetrical Cu-S₁N₃ structure. Theoretical analysis demonstrated that the asymmetric coordination environment effectively enhanced O₂ adsorption and facilitated the ORR performance. The g-Cu-SACs show excellent catalytic activity in alkaline oxygen reduction reaction with a half-wave potential of 0.920 V_{RHE} and good cycling stability, which are superior to that of three-dimensional copper single-atom catalysts (Cu-SACs, supported by N/S-codoped carbon framework directly derived from ZIF-8). Furthermore, the zinc-air battery assembled with g-Cu-SACs also exhibits high specific capacity and remarkable cycling lifetime. This work provides a novel strategy to construct highly exposed single-atom catalysts for energy-related applications.

1. Introduction

The electrocatalytic oxygen reduction reaction (ORR) plays a crucial role in energy-related devices, such as metal-air batteries and fuel cells [1–4]. However, the oxygen reduction process is severely limited by sluggish kinetics and insufficient operation durability [5–7]. Although platinum-based composites show excellent ORR catalytic activity, the scarcity and high-cost have severely limited their application [8,9]. Therefore, single-atom catalysts (SACs) with non-precious transition metal are emerging as the most promising alternative. The highly dispersed 3d transition-metal-nitrogen four-coordination moiety (M-N₄, M = Fe, Cu, Co, Ni, Mn etc.) are generally deemed as active centers for adsorbing O₂ molecules and catalyzing the subsequent ORR [10–12]. However, the intermediate adsorption on symmetrical M-N₄ structure generally suffers from high energy barrier [13,14]. Recently, the secondary heteroatom doping (e.g. S [15,16] B [17] P, [12,18] Se [19]) has

demonstrated an effective way to break the symmetrical M-N₄ structure and thus optimize the adsorption energy toward crucial intermediates. Particularly, the doped S atoms can adjust electron-withdrawing/donating properties and induce applicable interactions between catalytic sites and oxygen intermediate, further enhancing the reaction kinetics of SACs [20,21]. Nevertheless, the incorporation of S doping is still challenging for the following reasons: i) The S doping is more difficult due to its larger volume and lower charge transfer rate compared to N atoms [22]; ii) Additional S heteroatom dopants need to be added during the synthesis process, making the preparation process cumbersome and uncontrollable [23]. iii) It is difficult to achieve uniform and stable S doping in the existing process due to the pyrolysis of solid sulfur source [24,25]. Therefore, developing high-efficiency and facile synthesis method for S doping in SACs is of great significance for practical application.

Generally, the ORR catalytic performance of SACs is not only

* Corresponding authors.

E-mail addresses: yqzhu@bit.edu.cn (Y. Zhu), zoums@bit.edu.cn (M. Zou), cba@bit.edu.cn (C. Cao).

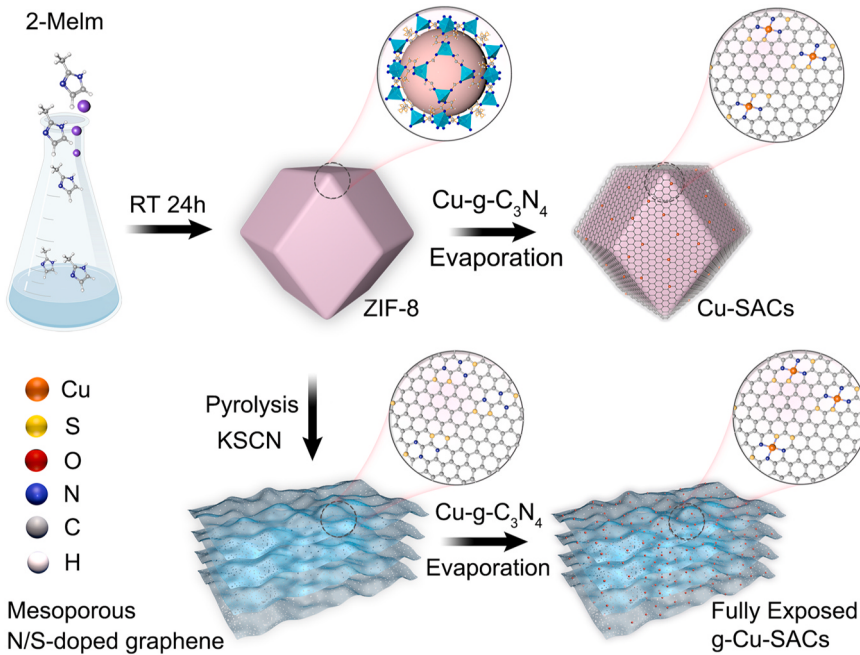


Fig. 1. Schematic illustration of fabrication for g-Cu-SACs including KSCN-assisted pyrolysis and volatilization-capture.

determined by the intrinsic activity of single catalytic site, but also the number of accessible active sites [22–27]. Morphology engineering of carbon support has been demonstrated as an effective strategy to boost the active site accessibility of SACs. Crystalline ZIF-8 is widely used to prepare various carbon supports for carrying single atoms benefitting from its ordered porous structure with high specific surface area [27, 28]. Moreover, the metal ions residing on ZIF-8 skeleton nodes can be isolated by organic linkers and converted into atomically dispersed atomic sites without aggregation during harsh pyrolysis process. However, catalysts derived from ZIF-8 are mostly geometrically collapsed three-dimensional (3D) structures dominated by out-of-order micro-pores, plenty of dead volume and blocked porous channels, in which only limited number active centers near outer surface are availability to reactant in ORR process, while a large amount of catalytic sites are hidden in carbon support, resulting in insufficient mass transport of O₂ reactant and H₂O product [29–31]. To address these issues, designing reasonable and favorable open structures has been proposed and demonstrated remarkable function by significantly increasing surface area to-volume ratio and maximizing exposure the metal sites, which can realize the interflow of solid-liquid-gas three-phase interfaces to improve the exposed active sites ratio, further promoting mass transfer [32,33]. For instance, Chen *et al.* reported a polymerization self-assembly method to prepare the ZIF8-derived carbon nanocage with dispersed metal single-atom sites and expressed enhanced ORR performance [33]. Yamauchi *et al.* utilized KCl and LiCl to exfoliate Zn-containing ZIF nanoleaves into ultra-thin graphene namomesh as anchoring support [34]. However, such methods can just realize the morphology regulation of the catalyst substrates but are unable to modulate the metal-atom configuration via heteroatom-introduction. Therefore, developing an effective strategy to simultaneously obtain controllable asymmetrical N/S-coordinated structure and increase active site accessibility is highly demanded but remain a challenge.

Herein, a novel and efficient dimensionality reduction strategy is reported for preparing mesoporous N/S-codoped graphene (denoted as N/SGr), in which the three-dimensional ZIF-8 octahedron is converted into two-dimensional ultrathin structures using KSCN as etching agent and a sulfur source for the first time. The as-prepared N/S-codoped graphene shows well-defined porous structure with interconnected channels, which endows a large specific surface area, and can be applied

as robust substrate for anchoring copper single-atom sites in g-Cu-SACs. Benefiting from the fully exposed Cu atoms and asymmetrical Cu-S₁N₃ coordinated structure, g-Cu-SACs exhibit prominent alkaline ORR properties with a half potential ($E_{1/2}$) of 0.920 V_{RHE}, far exceeding commercial Pt/C counterpart (0.845 V_{RHE}). Moreover, the assembled rechargeable zinc-air battery with obtained g-Cu-SACs exhibits an ideal peak power density of 110 mW cm⁻² and high specific capacity of 818.56 mAh g_{Zn}⁻¹, surpassing those of standard Pt/C counterpart in alkaline solution.

2. Experimental section

2.1. Synthesis of N/SGr and NC

The synthesis of zeolitic imidazolate frameworks (ZIF-8) followed a modified version of existing literature, see detail in [supplementary materials](#) [30]. The prepared ZIF-8 powder was thoroughly grounded with KSCN to achieve a homogeneous powder. And then, the mixture underwent heating at a rate of 5 °C/min in a tube furnace under an argon atmosphere, reaching 900 °C for a duration of 2 hours. The pyrolyzed product was etched by 2 M HCl at 80 °C for 12 hours under continuous stirring, then washed by water and dried to obtain N/SGr. For comparison, the prepared ZIF-8 were calcined directly to obtain NC via the same way as that employed for N/SGr. The ZIF-8 powder was placed into a ceramic boat and then transferred into the tube furnace, where it underwent thermal treatment at 900 °C for 2 hours with a heating rate of 5 °C/min under Ar gas to yield the NC.

2.2. Synthesis of Cu-g-C₃N₄ and g-C₃N₄

The synthesis of Cu-g-C₃N₄ involved the thermal treatment of a mixture containing 5 g melamine and 100 mg anhydrous copper chloride, which was firstly grounded and then heated at 600 °C (heating rate 5 °C/min) for 2 hours under Ar gas. On the other hand, the preparation for g-C₃N₄ followed the same procedure as Cu-g-C₃N₄, with the exception that anhydrous copper chloride was omitted from the mixture.

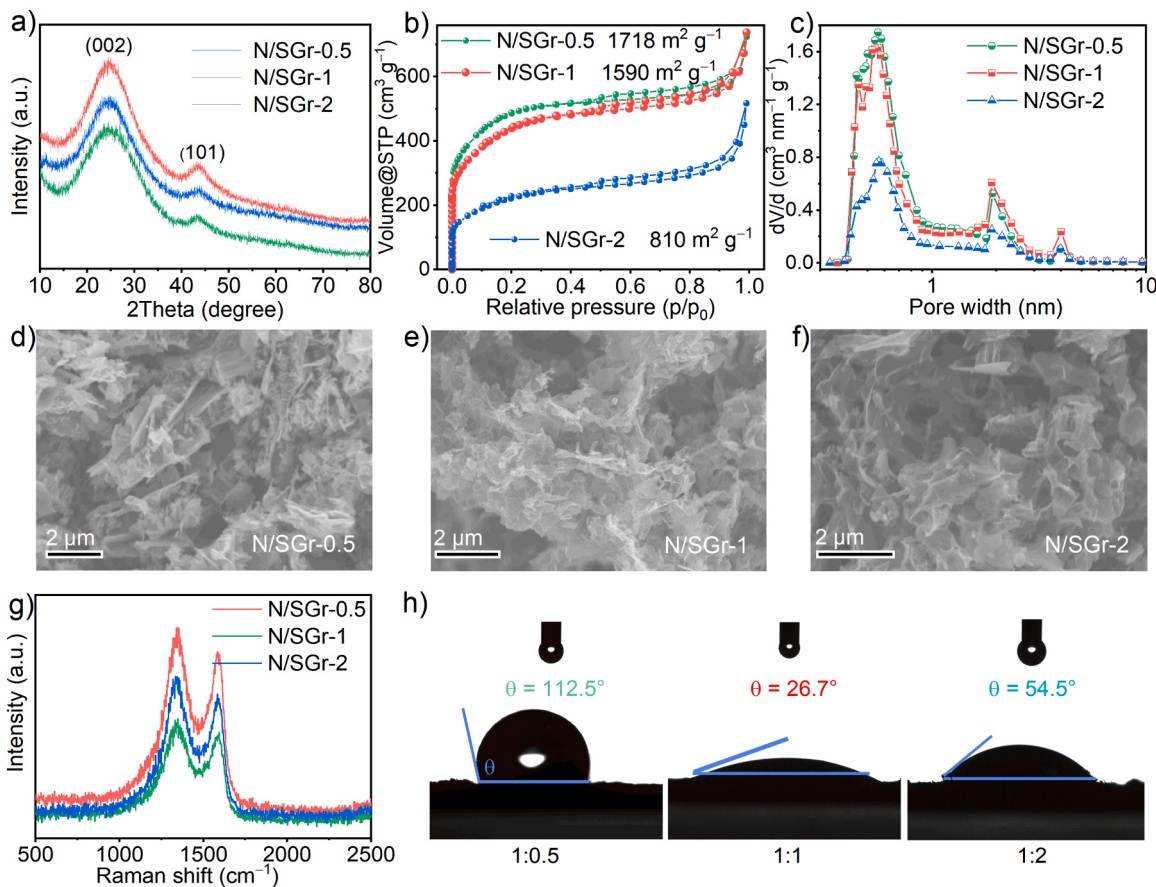


Fig. 2. Characterizations of N/S-codoped graphene (N/SGr-x, x = 0.5, 1 and 2). (a) XRD patterns. (b) and (c) Nitrogen adsorption-desorption isotherms and corresponding pore size distributions. (d-f) SEM images. (g) Raman spectra. (h) Contact angles.

2.3. Synthesis of g-Cu-SACs, Cu-SACs and SNC

Synthesis of g-Cu-SACs, Cu-SACs and SNC: 80 mg N/SGr-1 powder was fully mixed with 50 mg Cu-g-C₃N₄ and then heated at 900 °C (heating rate 5 °C/min) for 2 hours in Ar atmosphere to obtained g-Cu-SACs. For comparison, Cu-SACs were synthesized using NC and Cu-g-C₃N₄, via the same way as g-Cu-SACs. Similarly, SNC were prepared utilizing N/SGr-1 and g-C₃N₄ through the same method employed for g-Cu-SACs.

3. Results and

3.1. Structural analysis of N/SGr

The g-Cu-SACs were fabricated through a two-step approach of KSCN-assisted pyrolysis and volatilization-capture as depicted in Fig. 1. Firstly, the mesoporous N/S-co-doped graphene are obtained by mixing the prepared ZIF-8 precursors (Fig. S1) with KSCN salts by grinding

thoroughly and then pyrolyzed at high temperature. The molten KSCN salts are first used as etching agent and show remarkable effect in converting ZIF-8 octahedron into two-dimensional graphene. Simultaneously, S species in KSCN is incorporated as sulfur source and immobilized into graphene support. Previous work has shown that the incorporated K⁺ ions generally show obvious effects in the embedding and stripping of the derived carbon structure [35]. Secondly, copper salts were fully mixed with melamine by grinding and then converted to the pre-fabrication agent of Cu-contained graphitic carbon nitride (denoted as Cu-g-C₃N₄) at 600 °C (Fig. S2). Subsequently, the Cu-g-C₃N₄ was used as the volatilization source during the secondary heat-treatment. The mesoporous N/S-codoped graphene acted as

capture to anchor the copper atoms volatilized from Cu-g-C₃N₄ to form highly exposed copper single-atom catalysts. Simultaneously, the carbon substrate within Cu-g-C₃N₄ undergoes thermal decomposition and vaporization starting at 630 °C, with complete decomposition occurring at 750 °C [36]. By contrast, ZIF-8 precursors were directly pyrolyzed into three-dimensional carbon framework (Fig. S3) without KSCN etching to support the copper single-atom catalysts (Cu-SACs).

The etching effect of KSCN on the chemical composition and structure of mesoporous N/S-co-doped graphene was investigated through varying the weight ratio between etching agent and ZIF-8 precursor. X-ray diffractometry (XRD), scanning electron microscopy (SEM) and transmission electron microscopy (TEM) were employed to clarify the etching process of were employed to clarify the etching KSCN by analyzing the pre-pickling products. Fig. S4 suggest that the ZnS microcrystals are generated in the carbon layer. The subsequent pickling process involved the removal of ZnS crystals, resulting in the formation of abundant pores on the carbon matrix. As a result, N/SGr-x (x = 0.5, 1 and 2, corresponding to KSCN/ZIF-8 mass ratios of 0.5, 1 and 2, respectively) was successfully obtained. XRD patterns of N/SGr-0.5, N/SGr-1 and N/SGr-2 only exhibit two broad peaks attributed to (002) and (100) planes of graphitic carbon (Fig. 2a) [13,26]. It is worth noting that the (002) peaks of N/SGr-1 and N/SGr-2 exhibit increased broadness, indicating the presence of graphene sheets in these two samples, which could be further supported by SEM and TEM images of N/SGr-x obtained with different ratio of KSCN (Fig. 2d-e, and Fig. S5) [37,38]. Additionally, with the increasing of heating temperature, the amount of ZIF8-derived nanosheet gradually increased and reaches its maximum at 900 °C (Fig. S6a).

The N₂ sorption measurements demonstrated that N/SGr-x exhibits a type IV isotherm. The volume of absorption experiences a rapid increase

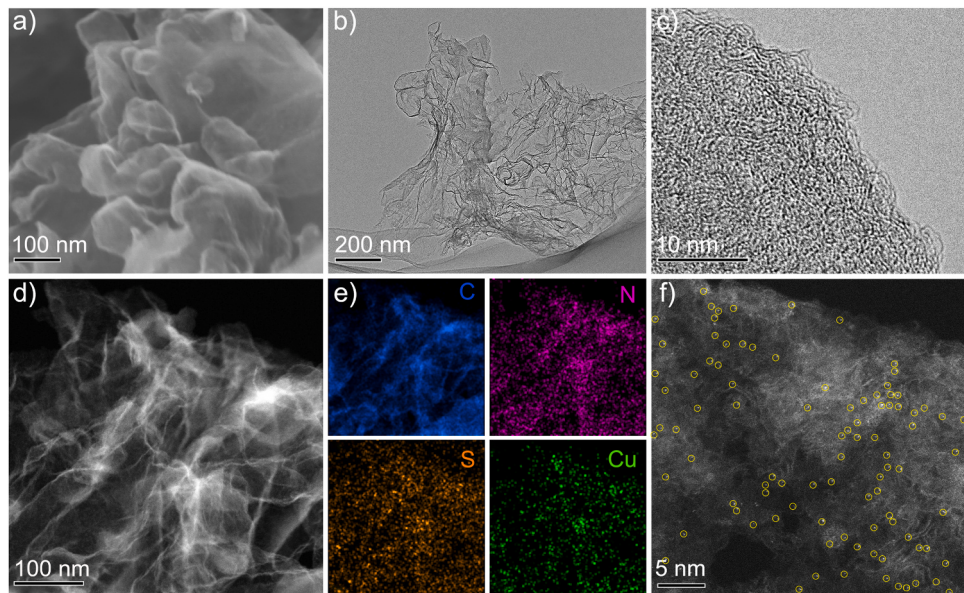


Fig. 3. Morphology and structure of g-Cu-SACs: (a) SEM image. (b) TEM image. (c) HRTEM image. (d,e) HAADF-STEM image and corresponding EDS elemental mapping. (f) Aberration-corrected HAADF-STEM image.

at low relative pressure ($P/P_0 < 0.02$) and exhibits a steep N_2 uptake during the relative pressure increasing to $0.4 < P/P_0 < 1$, indicating the coexistence of mesopores and micropores in N/SGr-x [39]. Fig. 2b, and

Table S1, show that their porosities mainly comprise one micropore and two mesoporous systems with sizes predominantly centered around 0.3, 2 and 4 nm, demonstrating the hierarchical porous feature of N/SGr-x,

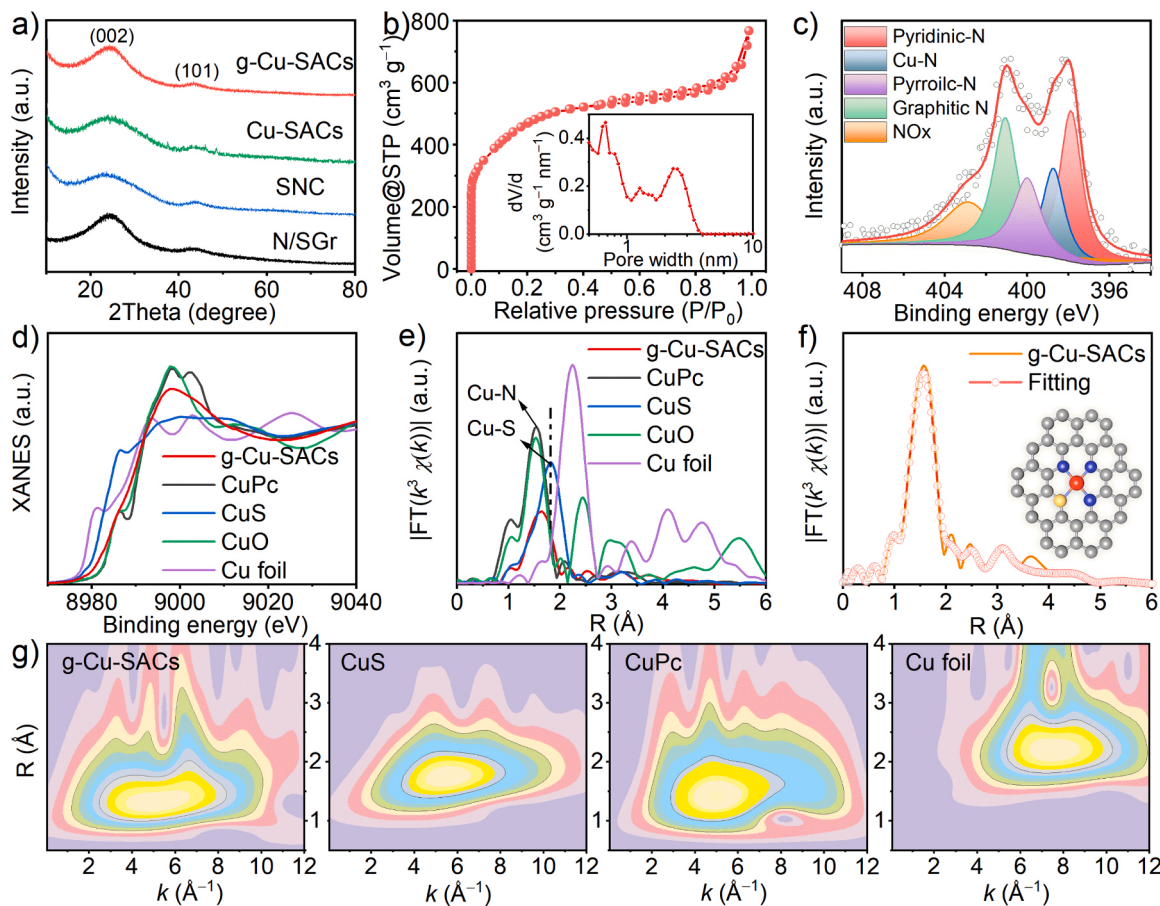


Fig. 4. Analysis of the atomic structure of g-Cu-SACs. (a) XRD patterns of the prepared catalysts. (b) N_2 adsorption-desorption isotherm. Inset: corresponding pore size distribution. (c) High-resolution XPS N 1 s spectra. (d) Cu K-edge XANES spectra. (e) FT k^3 -weighted Cu K-edge EXAFS spectra. (f) First shell (Cu-N) fitting of FT-EXAFS spectra at R space, (the insets are the fitted structures). (g) 3D contour WT-EXAFS plots.

which is obviously different from the single micropore system of NC derived from ZIF8 (Fig. S6b) [40]. It is worth noting that N/SGr-1 exhibits the most significant mesoporous content compared to the other two samples. Such phenomenon could be ascribed to the infusion of molten KSCN into ZIF-8 crystal, facilitating interaction with carbon and eliminating the compact carbon layer. Consequently, a porous structure is formed with an elevated specific surface area during the pyrolysis and carbonization process [41,42]. All samples possess both microporous and mesoporous structures, which endow leading to higher specific surface area compared to N-modified carbon (NC) (Table S1). Raman spectra were also utilized to analyze the lattice disorder of N/SGr-x [24]. As depicted in Fig. 2g, the I_D/I_G ratio of (N/SGr-0.5) (1.786), N/SGr-1 (1.765), and N/SGr-2 (1.777) exhibit a high degree of similarity, indicating a well-balanced presence of graphitic and defective carbon in the synthesized samples.

The contact angles of N/SGr-0.5, N/SGr-1 and N/SGr-2 are 112.5°, 26.7° and 54.5°, respectively, indicating that the surface of N/SGr-1 exhibits a higher degree of hydrophilicity, which could be benefit for promoting the OH^- adsorption (Fig. 2j) [43,44]. The X-ray photoelectron spectroscopy (XPS) survey results of N/SGr-x are presented in Fig. S7. High-resolution C 1 s spectra of N/SGr-x could be divided into three characteristic peaks, which could be ascribed to C-C=C (284.6 eV), C-N/C-S (285.8 eV) and C=O (288.9 eV), respectively (Fig. S8a) [22]. Additionally, the presence of C-SO_x-C (168.4 eV), C-S-C (165.3 eV), and C-S-C (164.1 eV) could be demonstrated in S 2p spectrums (Fig. S8b) [45]. The broad envelop in high-resolution N 1 s spectrums of N/SGr-x could be deconvolved into four characteristic

peaks of N types, including oxidized N, graphitic N, pyrrolic N and pyridinic N, respectively (Fig. S8c). The observation of C-N/C-S and C-S-C bonds indicate the successful incorporation of N and S dopants, wherein the extra S doping can induce long-range interactions and modulate bonds configuration of the single atom centers, which will be discussed in the following characterization [15,16].

3.2. Structural analysis of g-Cu-SACs

Given the fact that the micropores mainly offers catalytic active sites and the mesoporous structure could improve the mass transfer, the obtained N/SGr-1 with ideal micro/mesopores distribution was selected as the preferred carrier to support Cu atoms as ORR catalyst. SEM and TEM images of g-Cu-SACs display an ultrathin graphene structure (Fig. 3a and b). High

-resolution TEM (HRTEM) image shows typical amorphous structure with randomly oriented defective graphitic domains (Fig. 3c) [46–48]. Such structural features provide guarantee for enlarging the available active area for loading abundant catalytic sites. Subsequently, high-angle annular dark-field scanning TEM (HAADF-STEM) and corresponding elemental mapping results indicate that C, S, N, and Cu elements are uniformly dispersed throughout the entire graphene (Fig. 3d, e). Further, aberration-corrected HAADF-STEM was employed to directly visualize the atomic dispersion in g-Cu-SACs (Fig. 3f). The dispersion of abundant bright dots is observed on the g-Cu-SACs randomly, without any metal cluster or particles detected. The morphology and atomic structure characterization of Cu-SACs are also

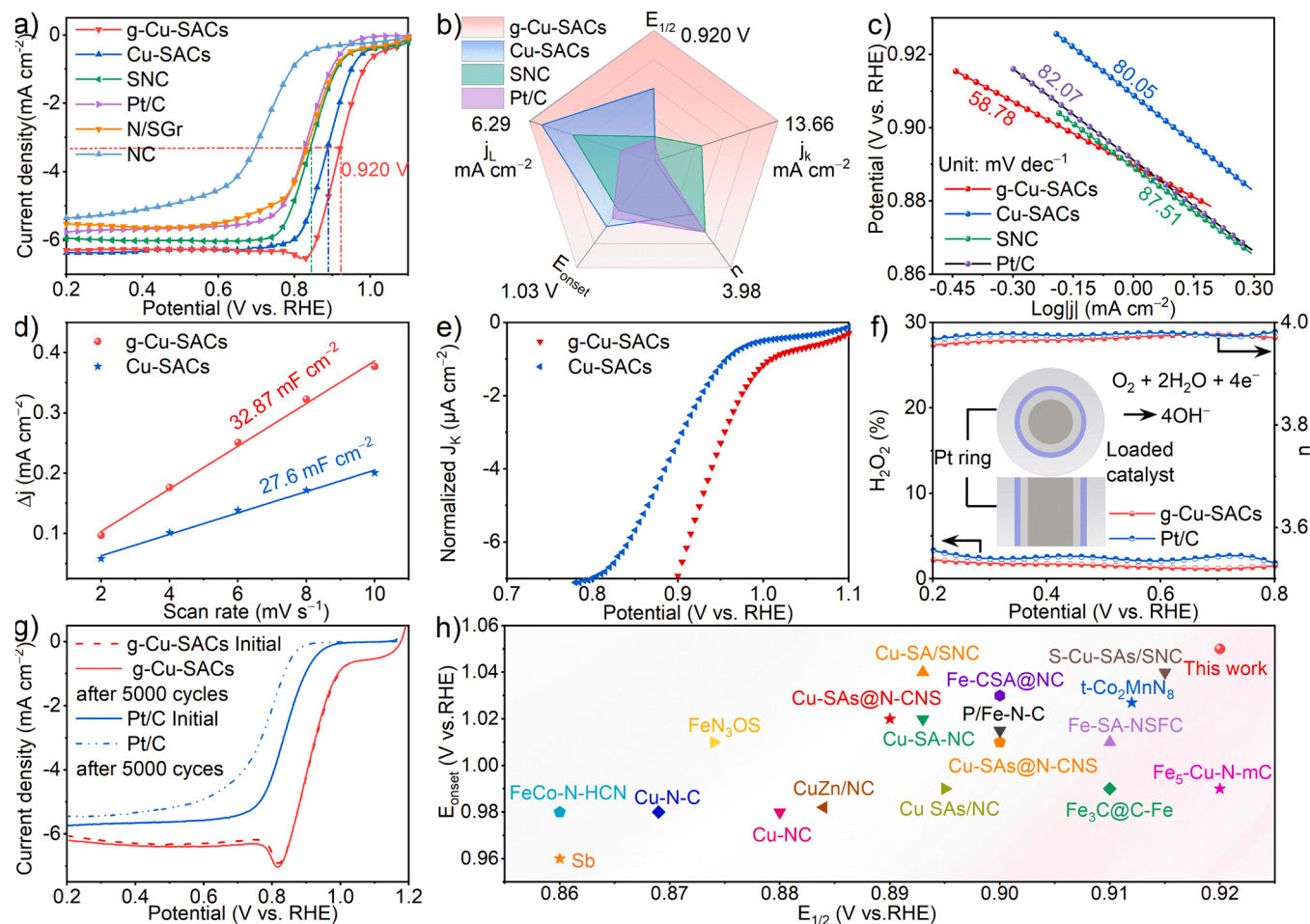


Fig. 5. (a) LSV curves at 1600 rpm. (b) Comparison of E_{onset} , $E_{1/2}$, j_L at 0.85 V vs. RHE, j_L , and electron transfer numbers (n). (c) Corresponding Tafel slopes O_2 -saturated 0.1 M KOH. (d) C_dL . (e) ECSA normalized kinetic current densities. (f) H_2O_2 yield and electron transfer number (n). (g) LSV curves before and after 5000 cycles. (h) Comparison of E_{onset} and $E_{1/2}$ between our catalyst and some recent reported ORR catalysts.

provided in [Fig. S9](#) and [Fig. S10](#) for comparison, demonstrating the absence of significant aggregation of Cu atoms within the Cu-SACs.

XRD patterns show typical amorphous nature without any bulk-like metallic phase observed, indicating the absence of metal atom agglomeration or cluster in the obtained g-Cu-SACs ([Fig. 4a](#)). The obtained catalysts are further heated to 1000 °C and no obvious crystal structures and morphology collapse can be observed, further demonstrating a good thermal stability of the fabricated catalysts ([Fig. S11](#)). Additionally, inductively coupled plasma mass spectroscopy (ICP-MS) analysis demonstrates the Cu content of 0.48 wt% in g-Cu-SACs ([Table S1](#)). N₂ adsorption-desorption isotherm results demonstrate that g-Cu-SACs possess an obviously larger surface area of 1612 m² g⁻¹ ([Fig. 4b](#)). In addition, a noticeable hysteresis can be observed in the obtained type IV isotherm curves, indicative of the mesopores existence with an approximate diameter of 3.3 nm. In particular, the g-Cu-SACs undergo further etching due to the gas released during Cu-g-C₃N₄ pyrolysis, resulting in a slight increase in specific surface area. XPS measurement was conducted to characterize the valance structure and chemical

composition of catalysts. The survey result reveals the existence of C, N, O, S and Cu elements in g-Cu-SACs ([Fig. S12](#) and [Table S2](#)). High-resolution XPS spectrum of N 1 s can be analyzed by a five-peak fitting model, including Cu-N (398.7 eV), pyridinic-N (397.8 eV), pyrrolic-N (400.4 eV), graphitic-N (401.1 eV) and oxidized-N (402.7 eV), respectively ([Fig. 4c](#)), in which graphitic-N and pyridinic-N are the dominant N species in g-Cu-SACs [26]. The specific proportions are as follows: 16.43% (Cu-N), 26.93% (pyridine-N), 15.52% (pyrrole-N), 25.2% for (graphite-N), and 16.46% (oxidized-N) ([Fig. S13](#)).

The X-ray absorption fine structure (XAFS), encompassing X-ray absorption near-edge structure (XANES) and extended X-ray absorption fine structure (EXAFS), has been occupied to further characterize the coordination and local chemical environment of atomically dispersed metal species [49,50]. Cu K-edge XANES spectra ([Fig. 4d](#) and [Fig. S15a](#)) shows that the near-edge energy adsorption threshold of g-Cu-SACs is located between the CuS and CuPc, implying that the valence state of Cu in g-Cu-SACs fall between those of these two counterparts. The Fourier-transformed (FT) k³-weighted EXAFS spectrum of g-Cu-SACs exhibit a prominent peak at 1.56 Å, which shows a positive shift compared to that of Cu-N/O bond. Such shift can be ascribed to the involvement of Cu-S bond, implying direct coordination between S and Cu atoms, which is consistent with the findings from XPS results ([Fig. S14](#)) [9,51]. In addition, no typical signals of Cu–Cu bonds is observed, indicative of the existence of dispersed atomic Cu sites without cluster formation in g-Cu-SACs ([Fig. 4e](#) and [Fig. S15b](#)). To establish correlations between FT-EXAFS peaks and K- and R-spaces, we employed 3D contour plots of wavelet transform X-ray absorption fine structure (WT-EXAFS), as depicted in [Fig. 4g](#). The maximum peak observed for g-Cu-SACs at (5.2 Å⁻¹, 1.25 Å) can be attributed to Cu-N and Cu-S coordination (Cu-N bond at 5.1 Å⁻¹, 1.46 Å, Cu-S bond at 5.6 Å⁻¹, 1.75 Å), which is different from the Cu foil (Cu-Cu bond at 8 Å⁻¹, 2.25 Å) ([Fig. 4g](#)). Additionally, distinct characteristics were observed for CuO and Cu₂O, where the Cu-O bond exhibited different properties at 6 Å⁻¹, 1.5 Å, and 6 Å⁻¹, 1.4 Å, respectively ([Fig. S15c, d](#)). These findings further confirm that individually isolated Cu site atoms are Cu site coordinated with N rather than O [52]. No observation of the maximum intensity at ≈ 8 Å⁻¹ in g-Cu-SACs also verifies the atomic dispersion without Cu-Cu. Quantitative least-squares EXAFS fitting of g-Cu-SACs was executed at the Cu K-edge to conclude the coordination structure in [Fig. 4f](#) and [Table S2](#). The obtained results show that the fitting EXAFS curve of the first shell of Cu is perfectly consistent with the experimental spectral curve ([Fig. 4f](#) and [Fig. S15e, f](#)), indicating that the Cu atoms in g-Cu-SACs display a coordination number of 4.0 ± 0.2 at the first coordination shell, and are connected with three N atoms and one S atom with the bond lengths of 2.48 and 1.98 Å, respectively ([Table S3](#)).

3.3. Electrocatalytic ORR performance

The electrochemical activities of g-Cu-SACs, Cu-SACs and commercial Pt/C counterparts (20%) were evaluated in alkaline media. The cycle voltammetry (CV) curve of g-Cu-SACs displays a noticeable reduction peak in O₂-saturated 0.1 M KOH solution, indicating that g-Cu-SACs shows obvious electrocatalytic activity for ORR ([Fig. S16](#)). Line scan voltammetry (LSV) measurements show that the g-Cu-SACs presents an exceptional performance, with a high positive onset potential ($E_{onset} = 1.03$ V) and half-wave potential ($E_{1/2} = 0.920$ V), which is much better than that of Cu-SACs ($E_{onset} = 1.01$ V, $E_{1/2} = 0.880$ V) ([Fig. 5a](#)). For comparison, the electrocatalytic properties of NC, N/SGr, S/N-co-doped carbon (SNC) have also been investigated and demonstrate inferior E_{onset} and $E_{1/2}$, suggesting that the involvement of Cu–N/S or Cu–N could be more significant in ORR catalysis within g-Cu-SACs and Cu-SACs catalysts, rather than relying on N–C or N–C–S interactions. Additionally, the $E_{1/2}$ of g-Cu-SACs exhibits a remarkable increase of 73 mV compared to that of standard Pt/C ($E_{onset} = 0.956$ V, $E_{1/2} = 0.847$ V). The $E_{1/2}$ and kinetic current density (j_k) at a potential of 0.85 V for the partial catalysts are summarized in [Fig. 5b](#). The optimal g-Cu-SACs exhibits the highest j_k of 13.66 mA cm⁻², compared to Pt/C (3.81 mA cm⁻²) and contrast samples, indicating the accelerated kinetics of the ORR process. However, the ORR properties of Cu-g-SACs in acidic media are relatively inferior to those of Pt/C ([Fig. S17](#)). Furthermore, the Tafel slope of g-Cu-SACs is the lowest (58.78 mV dec⁻¹) compared to all other catalysts synthesized in this study ([Fig. 5c](#)). The above results indicate that the coexistence of highly open graphene with hierarchical porous structure and asymmetric

coordination active sites significantly boosts the ORR activity of g-Cu-SACs. The electrochemical active specific surface area (ECSA) of catalysts is determined via calculating the double-layer capacitance (C_{dl}), which is an essential factor for characterizing the surface characteristics of catalyst. As shown in [Fig. 5d](#) and [Fig. S18](#), the g-Cu-SACs demonstrates an enhanced electrochemical double-layer capacitance (C_{dl}) of 32.87 mF cm⁻² compared to Cu-SACs (27.6 mF cm⁻²). This higher C_{dl} value further substantiates that a well-designed hierarchically porous architecture and a large specific surface area contribute favorably towards generating ample active sites on its surface, thus facilitating accelerated ORR kinetics [53,54]. Correspondingly, the ECSA-normalized j_k of the kinetic control region ([Fig. 5e](#)) additionally demonstrates that the g-Cu-SACs exhibits a higher slope, thereby further substantiating its superior ORR catalytic activity.

Rotating ring-disk electrode (RRDE) measurements ([Fig. 5f](#)) suggest that the g-Cu-SACs exhibit a H₂O₂ yield below 2% within 0.2–0.8 V, confirming a direct 4e⁻ transfer ORR process in alkaline media ($n \approx 3.98$). Similarly, Koutecky–Levich (K-L) plots also indicate the first-order reaction kinetics of dissolved oxygen and further prove the electron transfer number of 4, demonstrating a significant preference for reducing O₂ to H₂O with a selectivity 4e⁻ ([Fig. S19](#)) [55]. Aside from the ideal catalytic activity, substantial long-term stability is another essential indicator for a desirable ORR catalyst. Stability tests show that there are almost no decay for $E_{1/2}$ and limited current after 5000 continuous cycles ([Fig. 5g](#) and [Fig. S20](#)), indicating superior stability of g-Cu-SACs. In contrast, commercial Pt/C and Cu-SACs catalyst displays significant negative shifts after the durability test. After the stability test, the SEM and TEM images in [Fig. S21](#) indicate that the morphology and structure of g-Cu-SACs remained unaffected and there is no cluster/particle aggregation. Meanwhile, the AC HAADF-STEM images revealed that most single atoms were well maintained after cycling ([Fig. S21f](#)), providing further validation for the exceptional stability exhibited by g-Cu-SACs during the ORR process. In particular, the selected area electron diffraction (SAED) analysis confirmed the absence of phase/structure change in the catalyst after cycling ([Fig. S21c](#)). Additionally, we conducted XPS tests on the sample of post-durability test. It was observed that there was no evident change in the oxidation states ([Fig. S22](#)). All these findings collectively suggested that g-Cu-SACs exhibit a superior

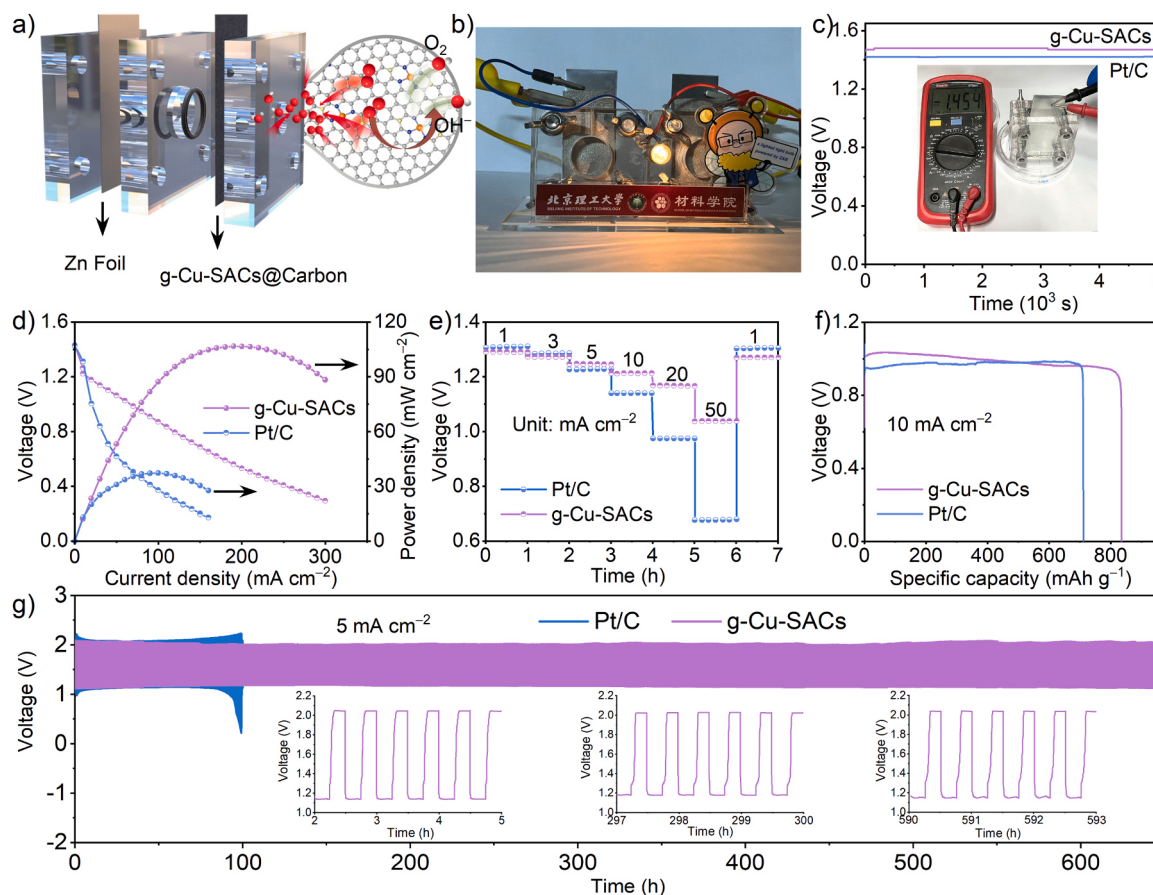


Fig. 6. (a) Schematic representation of rechargeable zinc-air battery assembled with g-Cu-SACs. (b) Digital photograph of light bulb illuminated by a pair of g-Cu-SACs-assembled batteries connected in sequence. (c) Open circuit voltage curves. (d) Discharge polarization curves and corresponding power density plots. (e) Galvanostatic discharge plots under different current densities. (f) Specific capacity output curves. (g) Continuous cycling curves of galvanostatic discharge-charge, with an inset illustrating the voltage efficiency (VE).

stability. Moreover, the g-Cu-SACs outperforms recently reported state-of-the-art non-precious metal electrocatalysts in terms of $E_{1/2}$ and n (Fig. 5h and Table S4). To assess the impact of fuel crossover, the chronoamperometric responses were recorded to evaluate the ORR when methanol was instantaneously introduced at approximately 300 seconds and contrasted with Pt/C catalyst. As depicted in Fig. S23, a notable decline in relative current for Pt/C is noticed, whereas that of g-Cu-SACs exhibit a minor alteration as methanol is introduced, suggesting that the catalyst is highly resistant to the impact of methanol crossover. The above results suggest that g-Cu-SACs show a 4e⁻ transfer mechanism in ORR, exceptional durability, and good anti-methanol toxicity with great potential for practical application.

3.4. Zinc-air battery performances

In order to evaluate the device application of g-Cu-SACs, the rechargeable liquid zinc-air battery (ZAB) was fabricated with g-Cu-SACs as the air cathode materials, Zn plate as anode, and 6 M KOH with 0.2 M Zn(CH₃COO)₂ as electrolyte (Fig. 6a). A LED display can be successfully powered for 4 h with remarkable brightness by a single g-Cu-SACs-assembled ZAB (Fig. S24). Two batteries in series can lighten a light bulb (1.5 V, 0.2 A) and show good working durability over 4 h (Fig. 6b). The measured open-circuit voltage (OCV) of g-Cu-SACs-assembled ZAB is up to 1.48 V (Fig. 6c), which is higher than that of Pt/C-based ZAB (1.42 V). Furthermore, g-Cu-SACs-assembled ZAB exhibits a significantly higher peak power density of 112 mW cm⁻² compared to Pt/C-based counterpart (Fig. 6d). Moreover, when the current density increases from 1 to 50 mA cm⁻², the g-Cu-SACs-assembled ZAB can

maintain considerably higher discharge voltage than that of Pt/C-based battery (Fig. 6e). Notably, the discharge voltage of g-Cu-SACs-assembled ZAB can be effectively restored upon returning the current density to 1 mA cm⁻², whereas a noticeable decline in voltage is evident in Pt/C-based ZAB, while the Pt/C-based ZAB shows an obvious voltage drop. The remarkable rate performance and satisfactory voltage restoration properties of g-Cu-SACs-assembled ZAB are attributed to the highly exposed active center and ultrathin mesoporous architecture of

g-Cu-SACs, which facilitate rapid ORR kinetics and minimize mass transfer resistance [56]. Furthermore, the specific capacities of the fabricated ZAB were determined through continuous galvanostatic discharge procedure at 10 mA cm⁻² and subsequently normalizing the results based on the consumed mass of zinc anode. The calculated specific capacities of ZAB based on g-Cu-SACs and Pt/C are 818.56 and 696.29 mAh g_{Zn}⁻¹, respectively (Fig. 6f). The remarkable improvement in specific capacity could be attributed to the exceptional 4e⁻ selectivity and enhanced ORR activity of g-Cu-SACs. A detailed comparison of battery performance further indicates that the as-obtained g-Cu-SACs can show superior device application (Table S5). The long-term charge-discharge performance of g-Cu-SACs-assembled ZAB was assessed to determine the cycling stability. As depicted in Fig. 6g, the g-Cu-SACs-assembled ZAB displays a remarkable cycling stability, with a maintain stable and small voltage gap ($\Delta V < 0.85$ V) for a duration of 650 hours at 5 mA cm⁻² while the Pt/C-based ZAB shows inferior cyclic stability by maintaining a significant voltage degradation and an increased voltage gap. These results demonstrate the appealing prospects of utilizing g-Cu-SACs in practical ZAB device for efficient energy conversion and storage applications [57]. Moreover, the recycled g-Cu-SACs remain

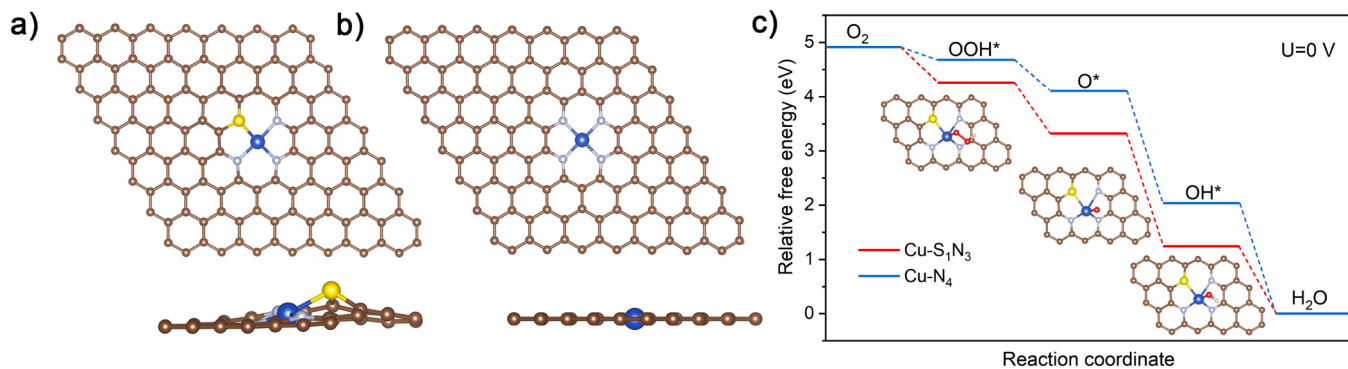


Fig. 7. DFT calculation of g-Cu-SACs. Optimized atomic structures of (a) Cu-S₁N₃, (b) Cu-N₄, (c) Gibbs free-energy diagram in the alkaline media, (the insets are the ORR elemental steps). Brown, blue, gray, yellow, red and pink balls represent C, Cu, N, S, O and H atoms, respectively.

nearly unchanged morphology and structure after prolonged cycling of 650 hours, as evidenced by TEM images (Fig. S25a-c). The HRTEM image reveals the excellent dispersion of Cu atoms without any visible agglomeration, indicating the robust structure of the g-Cu-SACs catalyst (Fig. S25d-h). This observation highlights the robust structural stability of g-Cu-SACs. These findings provide robust evidence for the exceptional potential of g-Cu-SACs as the promising substance in ZAB applications.

4. Theoretical calculation

To investigate the underlying mechanism of the enhanced ORR activity on g-Cu-SACs under alkaline conditions, Density functional theory (DFT) calculations were carried out to reveal the process of four-electron ORR reaction on various Cu-based structures incorporated within a carbon framework. As shown in Fig. 7a, b, the optimized Cu-N₄ and Cu-S₁N₃ structures were constructed based on XAFS data. During the ORR process, proton-coupled electron transfer facilitated the formation of proposed oxygen-containing intermediates (i.e., OOH^{*}, O^{*}, and OH^{*}) and the optimized adsorption-dissociation geometry on the two configurations is shown in the Fig. S26. As can be seen from the Gibbs free energy diagram in Fig. 7c, when the U=0 V_{RHE}, the free energy of all elementary reactions on the Cu-N₄ and Cu-S₁N₃ tends to decline, indicating that the process is spontaneous and exothermic. In comparison, it is observed that both Cu-N₄ and Cu-S₁N₃ exhibit a rate-determining step (RDS) of O₂ → OOH^{*}. Moreover, the free energy difference between the Cu-S₁N₃ and Cu-N₄ indicates that Cu-S₁N₃ configuration effectively enhances the adsorption of OOH^{*}, and thus improves the ORR activity. Therefore, it can be inferred that the introduction of Cu-S asymmetric coordination in the carbon matrix results in an asymmetrical charge distribution, thereby enhancing the activity of ORR, which is consistent with the experimental findings.

5. Conclusion

In summary, the KSCN-assisted pyrolysis technique is developed to convert three-dimensional ZIF-8 precursors into two-dimensional ultrathin mesoporous N/S-codoped graphene to capture and anchor atomically dispersed Cu sites as the excellent ORR catalysts. Highly open morphology, mesoporous structure, large specific surface area, and abundant availability of active sites enable the as-synthesized g-Cu-SACs with unprecedented ORR catalytic activity in 0.1 M KOH electrolytes. Electrochemical measurements suggest that the g-Cu-SACs can show high half-wave potential of 0.920 V_{RHE} compared to the commercially available Pt/C and the traditional Cu-SACs (supported by three-dimensional carbon framework directly derived from ZIF-8). The half-wave potential of the g-Cu-SACs can be maintained for 5000 cycles without E_{1/2} decay. In terms of practical applications, the zinc-air battery assembled with the g-Cu-SACs as the air cathodes exhibits an impressive specific capacity of 818.56 mAh g_{Zn}⁻¹ and exceptional cycling

stability for over 650 hours, surpassing both the benchmark Pt/C catalysts and previously reported non-precious-metal catalysts. This study not only presents a new strategy to exploit the full potential of single-atom catalysts with rationally modulated dimensions and pore structure but also develops highly efficient electrocatalyst for the energy-related catalysis.

CRediT authorship contribution statement

Lifen Yang: Conceptualization, Methodology, Investigation, Data curation, Validation, Writing – original draft, Writing – review & editing, Supervision. **Changliang Du:** Data analysis. **Jiachen Tian:** Data analysis. **Xiuyun Yao:** Data analysis. **Qianwei Zhang:** Data analysis. **Xilan Ma:** Data analysis. **Youqi Zhu:** Conceptualization, Supervision, Writing – review & editing. **Meishuai Zou:** Writing – review & editing, Supervision, Funding acquisition. **Chuanbao Cao:** Writing – review & editing, Supervision, Funding acquisition.

Declaration of Competing Interest

The authors declare that they have no known competing financial interests or personal relationships that could have appeared to influence the work reported in this paper.

Data Availability

Supporting Information

Acknowledgements

This work was financed by the National Natural Science Foundation of China (21371023 and 52173273) and Fundamental Research Funds for the Central Universities (2022CX11013).

Appendix A. Supporting information

Supplementary data associated with this article can be found in the online version at doi:10.1016/j.apcatb.2024.124190.

References

- [1] Y. Zeng, C. Li, B. Li, et al., Tuning the thermal activation atmosphere breaks the activity–stability trade-off of Fe–N–C oxygen reduction fuel cell catalysts, *Nat. Catal.* 6 (2023) 215–227.
- [2] S. Liu, C. Li, M. Zachman, Y. Zeng, et al., Atomically dispersed iron sites with a nitrogen–carbon coating as highly active and durable oxygen reduction catalysts for fuel cells, *Nat. Energy* 7 (2022) 652–663.
- [3] H. Lei, L. Ma, Q. Wan, Z. Huangfu, S. Tan, Z. Wang, W. Mai, Porous carbon nanofibers confined NiFe alloy nanoparticles as efficient bifunctional electrocatalysts for Zn-air batteries, *Nano Energy* 104 (2022) 107941.

[4] A. Wang, X. Zhang, S. Gao, C. Zhao, S. Kuang, S. Lu, J. Niu, G. Wang, W. Li, D. Chen, H. Zhang, X. Zhou, S. Zhang, B. Zhang, W. Wang, Fast-charging Zn-air batteries with long lifetime enabled by reconstructed amorphous multi-metallic sulfide, *Adv. Mater.* 34 (2022) 2204247.

[5] L. Yang, X. Yao, C. Du, Z. Han, M. Jin, S. Peng, X. Ma, Y. Zhu, M. Zou, C. Cao, Constructing delocalized electronic structures to motivate the oxygen reduction activity of zinc selenide for high-performance zinc-air battery, *Chem. Eng. J.* 481 (2024) 148598.

[6] X. Yao, Y. Zhu, T. Xia, Z. Han, C. Du, L. Yang, J. Tian, X. Ma, J. Hou, C. Cao, Tuning carbon defect in copper single-atom catalysts for efficient oxygen reduction, *Small* 19 (2023) 2301075.

[7] X. Feng, G. Chen, Z. Cui, R. Qin, W. Jiao, Z. Huang, Z. Shang, C. Ma, X. Zheng, Y. Han, W. Huang, Engineering electronic structure of nitrogen-carbon sites by sp^3 -hybridized carbon and incorporating chlorine to boost oxygen reduction activity, *Angew. Chem. Int. Ed.* 63 (2023) e202316314.

[8] H. Chung, D. Cullen, D. Higgins, B. Sneed, P. Zelenay, Direct atomic-level insight into the active sites of a high-performance PGM-free ORR catalyst, *Science* 357 (2017) 479–484.

[9] H. Shang, X. Zhou, J. Dong, A. Li, X. Zhao, Q. Liu, J. Pei, Z. Li, Z. Jiang, D. Zhou, L. Zheng, Y. Wang, J. Zhou, Z. Yang, R. Cao, R. Sarangi, T. Sun, X. Yang, X. Zheng, W. Yan, Z. Zhuang, J. Li, W. Chen, Y. Li, Engineering unsymmetrically coordinated Cu-S₁N₃ single atom sites with enhanced oxygen reduction activity, *Nat. Commun.* 11 (2020) 3049.

[10] P. Sabhapathy, P. Raghunath, A. Sabbah, I. Shown, K. Saheb Bayikadi, R. Xie, V. Krishnamoorthy, M. Lin, K. Chen, L. Chen, Axial chlorine induced electron delocalization in atomically dispersed FeN₄ electrocatalyst for oxygen reduction reaction with improved hydrogen peroxide tolerance, *Small* 19 (2023) 2303598.

[11] T. Sun, L. Xu, D. Wang, Y. Li, Metal organic frameworks derived single atom catalysts for electrocatalytic energy conversion, *Nano Res.* 12 (2019) 2067–2080.

[12] K. Yuan, D. Lützenkirchen-Hecht, L. Li, L. Shuai, Y. Li, R. Cao, M. Qiu, X. Zhuang, M. Leung, Y. Chen, U. Scherf, Boosting oxygen reduction of single iron active sites via geometric and electronic engineering: nitrogen and phosphorus dual coordination, *J. Am. Chem. Soc.* 142 (2020) 2404–2412.

[13] X. Yao, Y. Zhu, Z. Han, L. Yang, J. Tian, T. Xia, H. Peng, C. Cao, Solvent-mediated oxidative polymerization to atomically dispersed iron sites for oxygen reduction, *Appl. Catal. B* 331 (2023) 122675.

[14] Y. Li, Y. Ji, Y. Zhao, J. Chen, S. Zheng, X. Sang, B. Yang, Z. Li, L. Lei, Z. Wen, X. Feng, Y. Hou, Local Spin-State Tuning of Iron Single-Atom Electrocatalyst by S-Coordinated Doping for Kinetics-Boosted Ammonia Synthesis, *Adv. Mater.* 34 (2022) 2202240.

[15] L. Li, S. Huang, R. Cao, K. Yuan, C. Lu, B. Huang, X. Tang, T. Hu, X. Zhuang, Y. Chen, Optimizing Microenvironment of Asymmetric N, S-Coordinated Single-Atom Fe via Axial Fifth Coordination toward Efficient Oxygen Electroreduction, *Small* 18 (2022) 2105387.

[16] Z. Zhang, X. Zhao, S. Xi, L. Zhang, Z. Chen, Z. Zeng, M. Huang, H. Yang, B. Liu, S. Pennycook, P. Chen, Single-Atom Catalysts: atomically dispersed cobalt trifunctional electrocatalysts with tailored coordination environment for flexible rechargeable Zn-air battery and self-driven water splitting, *Adv. Energy Mater.* 10 (2020) 2002896.

[17] X. Chen, P. Ye, H. Wang, H. Huang, Y. Zhong, Y. Hu, Discriminating active B–N sites in coralloidal b, n dual-doped carbon nano-bundles for boosted Zn-ion storage capability, *Adv. Funct. Mater.* 33 (2023) 2212915.

[18] Y. Li, K. Zang, X. Duan, J. Luo, D. Chen, Boost oxygen reduction reaction performance by tuning the active sites in Fe-N-P-C catalysts. Nitrogen and phosphorus dual coordination, *J. Energy Chem.* 55 (2021) 572–579.

[19] Z. Sun, H. Zhang, L. Cao, X. Liu, D. Wu, X. Shen, X. Zhang, Z. Chen, S. Ru, X. Zhu, Z. Xia, Q. Luo, F. Xu, T. Yao, Understanding synergistic catalysis on Cu-Se dual atom sites via operando X-ray absorption spectroscopy in oxygen reduction reaction, *Angew. Chem. Int. Ed.* 62 (2023) e202217719.

[20] L. Guo, S. Hwang, B. Li, F. Yang, M. Wang, M. Chen, X. Yang, S. Karakalos, D. Cullen, Z. Feng, G. Wang, G. Wu, Hui Xu, Promoting atomically dispersed MnN₄ sites via sulfur doping for oxygen reduction: unveiling intrinsic activity and degradation in fuel cells, *ACS Nano* 15 (2021) 6886–6899.

[21] Q. Li, W. Chen, H. Xiao, Y. Gong, Z. Li, L. Zheng, X. Zheng, W. Yan, W. Cheong, R. Shen, N. Fu, L. Gu, Z. Zhuang, C. Chen, D. Wang, Q. Peng, J. Li, Y. Li, Fe isolated single atoms on S, N codoped carbon by copolymer pyrolysis strategy for highly efficient oxygen reduction reaction, *Adv. Mater.* 30 (2018) 1800588.

[22] X. Li, X. Li, X. Yang, L. Liu, H. Zhao, Y. Li, H. Zhu, Y. Chen, S. Guo, Y. Liu, Q. Tan, G. Wu, Chemical vapor deposition for N/S-doped single Fe site catalysts for the oxygen reduction in direct methanol fuel cells, *ACS Catal.* 11 (2021) 7450–7459.

[23] Z. Chen, X. Peng, Z. Chen, T. Li, R. Zou, G. Shi, Y. Huang, P. Cui, J. Yu, Y. Chen, X. Chi, K. Loh, Z. Liu, X. Li, L. Zhong, J. Lu, Mass production of sulfur-tuned single-atom catalysts for Zn-air batteries, *Adv. Mater.* 35 (2023) 2209948.

[24] N. Shaji, C. Ho, M. Nanthagopal, P. Santhoshkumar, G. Sim, C. Lee, Biowaste-derived heteroatoms-doped carbon for sustainable sodium-ion storage, *J. Alloy. Compd.* 872 (2021) 159670.

[25] D. Zhang, H. Zhang, F. Gao, G. Huang, Z. Shang, C. Gao, X. Chen, J. Wei, M. Terrones, Y. Wang, Dual activation for tuning N, S Co-doping in porous carbon sheets toward superior sodium ion storage, *Small* (2024) 2308684.

[26] L. Yang, Y. Zhu, X. Yao, C. Du, Z. Han, J. Tian, X. Liu, X. Ma, C. Cao, Surface-optimized carbon nanocages with tailororable atomic Fe-N₄ sites to boost oxygen reduction in long stable zinc-air battery, *Energy Storage Mater.* 63 (2023) 102972.

[27] H. Huang, K. Shen, F. Chen, Y. Li, Metal-organic frameworks as a good platform for the fabrication of single-atom catalysts, *ACS Catal.* 10 (2020) 6579.

[28] C. Wang, J. Kim, J. Tang, M. Kim, H. Lim, V. Malgras, J. You, Q. Xu, J. Li, Y. Yamauchi, New strategies for novel MOF-derived carbon materials based on nanoarchitectures, *Chem* 6 (2020) 19.

[29] P. Sun, Z. Qiao, S. Wang, D. Li, X. Liu, Q. Zhang, L. Zheng, Z. Zhuang, D. Cao, Atomically dispersed zn-pyrrolic-n4 cathode catalysts for hydrogen fuel cells, *Angew. Chem. Int. Ed.* 62 (2022) e202216041.

[30] J. Tian, Y. Zhu, M. Hou, S. Zhang, X. Yao, L. Yang, C. Du, Z. Lv, X. Ma, C. Cao, Chemical vapor deposition towards atomically dispersed iron catalysts for efficient oxygen reduction, *J. Mater. Chem. A* 11 (2023) 5288–5295.

[31] Z. Han, Y. Zhu, X. Yao, H. Peng, C. Du, J. Tian, L. Yang, X. Ma, J. Hou, C. Cao, Boosting oxygen reduction of single-atomic iron sites by charge redistribution, *Appl. Catal. B*, 337 (2023) 122961.

[32] X. Tang, Y. Wei, W. Zhai, Y. Wu, T. Hu, K. Yuan, Y. Chen, Carbon nanocage with maximum utilization of atomically dispersed iron as efficient oxygen electroreduction nanoreactor, *Adv. Mater.* 35 (2023) 2208942.

[33] M. Qiao, Y. Wang, Q. Wang, G. Hu, X. Mamat, S. Zhang, S. Wang, Hierarchically ordered porous carbon with atomically dispersed FeN₄ for ultraefficient oxygen reduction reaction in proton-exchange membrane fuel cells, *Angew. Chem. Int. Ed.* 59 (2020) 2688.

[34] J. Li, W. Xia, J. Tang, Y. Gao, C. Jiang, Y. Jia, T. Chen, Z. Hou, R. Qi, D. Jiang, T. Asahi, X. Xu, T. Wang, J. He, Y. Yamauchi, Metal-organic framework-derived graphene mesh: a robust scaffold for highly exposed Fe–N₄ active sites toward an excellent oxygen reduction catalyst in acid media, *J. Am. Chem. Soc.* 144 (2022) 9280–9291.

[35] K. Wang, Z. Lu, J. Lei, Z. Liu, Y. Li, Y. Cao, Modulation of ligand fields in a single-atom site by the molten salt strategy for enhanced oxygen bifunctional activity for zinc-air batteries, *ACS Nano* 16 (2022) 11944–11956.

[36] J. Ban, X. Wen, H. Xu, Z. Wang, X. Liu, G. Cao, G. Shao, J. Hu, Dual Evolution in Defect and Morphology of Single-Atom Dispersed Carbon Based Oxygen Electrocatalyst, *Adv. Funct. Mater.* 31 (2021) 2010472.

[37] Q. Wang, Q. Wang, Y. Ji, Y. Lei, Y. Wang, Y. Wang, Y. Li, S. Wang, Pyridinic-N-dominated doped defective graphene as a superior oxygen electrocatalyst for ultrahigh-energy-density Zn-air batteries, *ACS Energy Lett.* 3 (2018) 1183.

[38] Z. Li, H. Cheng, Y. Lu, T. Wang, Y. Li, W. Zhang, G. He, Z. Tian, Potent charge-trapping for boosted electrocatalytic oxygen reduction, *Adv. Energy Mater.* 13 (2023) 2203963.

[39] C. Hou, L. Zou, L. Sun, K. Zhang, Z. Liu, Y. Li, C. Li, R. Zou, J. Yu, Q. Xu, Single-atom iron catalysts on overhang-eave carbon cages for high-performance oxygen reduction reaction, *Angew. Chem. Int. Ed.* 59 (2020) 7384.

[40] Z. Ye, Y. Jiang, T. Yang, L. Li, F. Wu, R. Chen, Engineering catalytic CoSe-ZnSe heterojunctions anchored on graphene aerogels for bidirectional sulfur conversion reactions, *Adv. Sci.* 9 (2022) 2103456.

[41] L. Zou, G. Zhong, Y. Nie, Z. Tan, W. Liao, X. Fu, Z. Pan, Porous carbon nanosheets derived from ZIF-8 treated with KCl as highly efficient electrocatalysts for the oxygen reduction reaction, *Energy Technol.* 9 (2021) 2100035.

[42] L. Chen, G. Shi, J. Shen, B. Peng, B. Zhang, Y. Wang, F. Bian, J. Wang, Deyuan Li, Z. Qian, G. Xu, G. Liu, J. Zeng, L. Zhang, Y. Yang, G. Zhou, M. Wu, W. Jin, J. Li, H. Fang, Ion sieving in graphene oxide membranes via cationic control of interlayer spacing, *Nature* 550 (2017) 380.

[43] S. Huo, X. Song, Y. Zhao, W. Ni, H. Wang, K. Li, Insight into the significant contribution of intrinsic carbon defects for the high-performance capacitive desalination of brackish water, *J. Mater. Chem. A* 8 (2020) 19927–19937.

[44] P. Shao, S. Yu, X. Duan, L. Yang, H. Shi, L. Ding, J. Tian, L. Yang, X. Luo, S. Wang, Potential difference driving electron transfer via defective carbon nanotubes toward selective oxidation of organic micropollutants, *Environ. Sci. Technol.* 54 (2020) 8464–8472.

[45] Y. Jia, X. Xiong, D. Wang, X. Duan, K. Sun, Y. Li, L. Zheng, Wenfeng Lin, M. Dong, G. Zhang, W. Liu, X. Sun, Atomically dispersed Fe-N₄ modified with precisely located S for highly efficient oxygen reduction, *Nano-Micro Lett.* 12 (2020) 116.

[46] X. Zhao, X. Zou, X. Yan, C. Brown, Z. Chen, G. Zhu, X. Yao, Defect-driven oxygen reduction reaction (ORR) of carbon without any element doping, *Inorg. Chem. Front.* 3 (2016) 417–421.

[47] Y. Li, S. Wang, X. Wang, Y. He, Q. Wang, Y. Li, M. Li, G. Yang, J. Yi, H. Lin, D. Huang, L. Li, H. Chen, J. Ye, Facile top-down strategy for direct metal atomization and coordination achieving a high turnover number in CO₂ photoreduction, *J. Am. Chem. Soc.* 142 (2020) 19259.

[48] X. Gong, J. Zhu, J. Li, R. Gao, Q. Zhou, Z. Zhang, H. Dou, J. Zhao, X. Sui, J. Cai, Y. Zhang, B. Liu, Y. Hu, A. Yu, S. Sun, Z. Wang, Z. Chen, Self-templated hierarchically porous carbon nanorods embedded with atomic Fe-N₄ active sites as efficient oxygen reduction electrocatalysts in Zn-air batteries, *Adv. Funct. Mater.* 31 (2021) 2008085.

[49] M. Tong, F. Sun, Y. Xie, Y. Wang, Y. Yang, C. Tian, L. Wang, H. Fu, Operando cooperated catalytic mechanism of atomically dispersed Cu@N₄ and Zn@N₄ for promoting oxygen reduction reaction, *Angew. Chem. Int. Ed.* 60 (2021) 14005–14012.

[50] C. Abney, R. Mayes, M. Piechowicz, Z. Lin, V. Bryantsev, G. Veith, S. Dai, W. Lin, XAFS investigation of polyamidoxime-bound uranyl contests the paradigm from small molecule studies, *Energy Environ. Sci.* 9 (2016) 448.

[51] H. Fei, J. Dong, M. Arellano-Jiménez, G. Ye, N. Kim, E. Samuel, Z. Peng, Z. Zhu, F. Qin, J. Bao, M. Yacaman, P. Ajayan, D. Chen, J. Tour, Atomic cobalt on nitrogen-doped graphene for hydrogen generation, *Nat. Commun.* 6 (2015) 8668.

[52] H. Yin, F. Dong, D. Wang, J. Li, Coupling Cu single atoms and phase junction for photocatalytic CO₂ reduction with 100% CO selectivity, *ACS Catal.* 12 (2022) 14096–14105.

[53] L. Yang, X. Zhang, L. Yu, J. Hou, Z. Zhou, R. Lv, Atomic Fe–N₄/C in flexible carbon fiber membrane as binder-free air cathode for Zn–air batteries with stable cycling over 1000h, *Adv. Mater.* 34 (2022) 2105410.

[54] J. Li, M.T. Sougrati, A. Zitolo, J.M. Ablett, I.C. Oğuz, T. Mineva, I. Matanovic, P. Atanssov, Y. Huang, I. Zenyuk, A.D. Cicco, K. Kumar, L. Dubau, F. Maillard, G. Dražić, F. Jaouen, Identification of durable and non-durable FeN_x sites in Fe–N–C materials for proton exchange membrane fuel cells, *Nat. Catal.* 4 (2021) 10–19.

[55] T. Gao, C. Zhou, Y. Zhang, Z. Jin, H. Yuan, D. Xiao, Ultra-fast pyrolysis of ferrocene to form Fe/C heterostructures as robust oxygen evolution electrocatalysts, *J. Mater. Chem. A* 6 (2018) 21577–21584.

[56] X. Ao, W. Zhang, B. Zhao, Y. Ding, G. Nam, L. Soule, A. Abdelhafiz, C. Wang, M. Liu, Atomically dispersed Fe–N–C decorated with Pt-alloy core–shell nanoparticles for improved activity and durability towards oxygen reduction, *Energy Environ. Sci.* 13 (2020) 3032–3040.

[57] X. Wang, Y. Jia, X. Mao, D. Liu, W. He, J. Li, J. Liu, X. Yan, J. Chen, L. Song, A. Du, X. Yao, Edge-rich Fe–N₄ active sites in defective carbon for oxygen reduction catalysis, *Adv. Mater.* 32 (2020) 2000966.